Transparent and Flexible $Mn_{1-x-y}(Ce_xLa_y)O_{2-\delta}$ Ultrathin-Film Device for Highly-Stable Pseudocapacitance Application

Samane Maroufi,* Rasoul Khayyam Nekouei, Sajjad S. Mofarah, Anthony P. O'Mullane, Yin Yao, Sean Lim, Claudio Cazorla, and Veena Sahajwalla

Control over the fabrication of state-of-the-art portable pseudocapacitors with the desired transparency, mechanical flexibility, capacitance, and durability is challenging, but if resolved will have fundamental implications. Here, defect-rich $Mn_{1-x-y}(Ce_xLa_y)O_{2-\delta}$ ultrathin films with controllable thicknesses (5–627 nm) and transmittance (≈29–100%) are fabricated via an electrochemical chronoamperometric deposition using a aqueous precursor derived from end-of-life nickel-metal hydride batteries. Due to percolation impacts on the optoelectronic properties of ultrathin films, a representative $Mn_{1-x-y}(Ce_xLa_y)O_{2-\delta}$ film with 86% transmittance exhibits an outstanding areal capacitance of 3.4 mF cm^{-2}, mainly attributed to the intercalation/de-intercalation of anionic O^{2-} through the atomic tunnels of the stratified $Mn_{1-x-y}(Ce_xLa_y)O_{2-\delta}$ crystallites. Furthermore, the $Mn_{1-x-y}(Ce_xLa_y)O_{2-\delta}$ thin-film device exhibits excellent capacitance retention of ≈90% after 16 000 cycles. Such stability is associated with intervalence charge transfer occurring among interstitial Ce/La cations and Mn oxidation states within the $Mn_{1-x-y}(Ce_xLa_y)O_{2-\delta}$ structure. The energy and power densities of the transparent flexible $Mn_{1-x-y}(Ce_xLa_y)O_{2-\delta}$ full-cell pseudocapacitor device, is measured to be 0.088 μWh cm^{-2} and 843 μW cm^{-2}, respectively. These values show insignificant changes under vigorous twisting and bending to 45–180° confirming these value-added materials are intriguing alternatives for size-sensitive energy storage devices.

Dr. S. Maroufi, Dr. R. Khayyam Nekouei, Dr. S. S. Mofarah,
Prof. V. Sahajwalla
Centre for Sustainable Materials Research and Technology
SMaRT@UNSW
School of Materials Science and Engineering
UNSW Sydney
Sydney, NSW 2052, Australia
E-mail: s.maroufi@unsw.edu.au
Prof. A. P. O'Mullane
School of Chemistry and Physics
Queensland University of Technology (QUT)
Brisbane, QLD 4001, Australia
Dr. Y. Yao, S. Lim
Electron Microscopy Unit (EMU)
Mark Wainwright Analytical Centre
UNSW Sydney
Sydney, NSW 2052, Australia
Dr. C. Cazorla
Departament de Física
Universitat Politècnica de Catalunya
Campus Nord B4-B5, Barcelona E-08034, Spain

The ORCID identification number(s) for the author(s) of this article can be found under https://doi.org/10.1002/adfm.202100880.

1. Introduction

Transparent and flexible energy storage devices are critical components in portable power-integrated electronic systems[1,2] such as shape-conformable sensors, flexible displays, capacitive touch screens, and solar cells.[3–6] Compared to other energy storage devices, pseudo and supercapacitors are known as ideal candidates for implementing such flexible and transparent characteristics due to their multifunctional properties and excellent features, including high power density, fast charge/discharge rate, and long cycling life.[7] Conductivity, mechanical flexibility, transparency, electrochemical capacitance, and durability of the used materials determine the performance of such energy storage devices.[7] To meet these criteria, candidate materials need to be designed in a 2D architecture. To date, several examples of flexible and transparent capacitors have been reported[7] which can be classified into the following subgroups: I) uniform ultrathin films fabricated from a range of materials such as graphene,[8–13] MXene[14,15] (namely 2D transition metal carbides, nitrides, or carbonitrides), conductive polymers,[4,16–19] transition metal oxides (TMOs) such as MnO_2,[20] NiO[21,22] Co_3O_4,[7] RuO_2,[23] and WO_3[24] II) 1D nanomaterials interlaced films from CNTs[25,26] and metal nanowires,[13,27,28] III) irregular mesh-like films,[29] IV) orderly patterned films,[3,30–34] and V) interdigitated patterned films.[35–38]

Among these, uniform ultrathin films hold greater promise due to their high stability under severe twisting, strong adherence to the surface, and cost-effectiveness for high-yield fabrication.[39–42] Furthermore, TMOs, by far, exhibit superior energy density relative to those of carbon-based materials. This is owing to their intrinsic high theoretical capacitances, multivalence oxidation states, and rapid redox reactions. Nonetheless, reproducible fabrication of these materials with controllable thickness, their intrinsic low conductivity, and poor cycling stability limit their widespread uses in flexible and size-sensitive pseudocapacitance applications. One of the promising approaches to overcome such shortcomings is engineering the bandgap alignment to improve ionic and electronic conductivities by the formation of substitution or interstitial atomic defects using extrinsic ions.[4]

Here we demonstrate an electrochemical-based synthesis method to fabricate defect-rich ultrathin $Mn_{1-x-y}(Ce_xLa_y)O_{2-\delta}$ films of tailored thicknesses. The as-synthesized films, which are derived from electronic waste (e-waste, i.e., end-of-life nickel-metal hybrid batteries) precursors, were made of atomically thin nanosheets and exhibited high mechanical flexibility, transparency, and large density of mixed oxidation states. The electrochemical performance of the films showed promising areal and gravimetric capacitances and exceptional long-term cycling stability. The energy and power densities of the $Mn_{1-x-y}(Ce_xLa_y)O_{2-\delta}$ symmetric pseudocapacitor device were also measured to be 0.088 µWh cm^{-2} and 843 µW cm^{-2}, respectively, which remained unchanged after vigorous bending and twisting. The present work enhances the application of flexible defect-rich TMO-based pseudocapacitors for transparent portable electronic devices, where superior durability can be obtained through controllable design of the architecture and structure.

2. Results and Discussion

2.1. Synthesis and Characterization of Defect-Rich $Mn_{1-x-y}(Ce_xLa_y)O_{2-\delta}$ Ultrathin Films

The fabrication of ultrathin films involves selective electrodeposition of dissolved cationic species using a polarization-based anodic chronoamperometric technique in an aqueous precursor derived from end-of-life nickel metal hydride batteries, as schematically shown in Figure S1a, Supporting Information. The electrolyte, which was obtained by an e-waste recovery process, consisted of Ce^{3+}, Mn^{2+}, and La^{3+} ions (Table S1, Supporting Information). To obtain the optimum voltage for film deposition, where co-oxidation of Ce^{3+} and Mn^{2+} ions occur, cyclic voltammetry (CV) analysis was carried out within a potential range of 0.0–1.0 V versus standard calomel electrode (SCE) (0.38–1.38 V vs RHE) at a pH of 2.5. The resulting CV (blue curve) is shown in **Figure 1**a, where the increase in anodic current with a shoulder at 0.92 V and a well-defined reduction peak at 0.72 V are attributed to the $Mn^{2+} \leftrightarrow Mn^{4+}$ reactions.

Thermodynamic calculations of the $Ce^{3+} \rightarrow Ce^{4+}$ oxidation reaction using speciation and Pourbaix diagrams revealed that the formation of CeO_2 may occur at potentials ≈0.6 V versus SCE. This is verified with the experimental CV results (red voltammogram in Figure 1a). The current density, which is an indication of the mass deposition, for Ce^{3+} oxidation is in the order of µA, is much lower than that for Mn^{2+} oxidation (mA), suggesting that the MnO_2-based structure is the main phase deposited. Furthermore, the water oxidation reaction, which occurs at $E_{H_2O/O_2} = 1.23$ V vs RHE, should be avoided and therefore the optimum voltage for the synthesis of MnO_{2-x} (oxidation of aqueous Mn^{2+}) was found to be 0.92 V vs SCE (1.3 V vs RHE). This applied potential still avoids water oxidation given the large overpotential associated with this reaction.

Although anodic deposition requires direct oxidation through a faradic process, a high concentration of La^{3+} (≈72 times more than Mn^{2+} and ≈8 times more than Ce^{3+}) present in the electrolyte can result in entrapment of La^{3+} in the as-crystallized $Mn_{1-x}(Ce_x)O_{2-\delta}$, during the co-oxidation of Ce^{3+} and Mn^{2+}. Despite the presence of Ni and Nd ions in the electrolyte precursor, the time-of-flight secondary ion mass spectroscopy's (TOF-SIMS) depth profile of the film (Figure S2a, Supporting Information) reveals no deposition of these two elements. The depth profile of atomic concentrations of the elements obtained by X-ray photoelectron spectrometer (XPS) is shown in Figure S2b, Supporting Information, where the concentrations of Mn, Ce, La, and O are measured to be 45.6–46.9, 3.2–3.8, 2.8–3.2, and 46.4–47.8 at%, respectively.

The chemical structure of the ultrathin film was characterized using Raman microspectra, the data of which is shown in Figure S3, Supporting Information. The three predominant bands, indicated by a magenta color, centered at 504, 568, and 639 cm^{-1} are related to the Mn-O in-plane/out-of-plane stretching vibration of δ-MnO$_2$.[43,44] The deconvoluted bands (blue) positioned at 386, 580, 649 and the band (orange) at 723 cm^{-1} are assigned to vibrational modes of E_1 and A_{2g} corresponding to α- and β- phases of MnO$_2$, respectively.[45,46] The mode at 606 cm^{-1} is associated with Mn-O stretching vibrations of Mn$_2$O$_3$,[47] which is only present for the $Mn_{1-x-y}(Ce_xLa_y)O_{2-\delta}$ structure. The Raman characteristic peaks associated with CeO$_2$ and La$_2$O$_3$ structures were not found. Nonetheless, comparing the Raman spectrum of pristine MnO$_{2-x}$ with that of the $Mn_{1-x-y}(Ce_xLa_y)O_{2-\delta}$, shown in Figure S3, Supporting Information, partial phase transformation of δ-MnO$_2$ to α- and β- phases can be attributed to the presence of La^{3+} and Ce^{3+}.

According to Hume–Rothery's rule for substantial solid solubility, the large ionic size mismatches of 74 and 65% for La^{3+}, with an ionic radius of 0.1172 nm, and Ce^{4+}, with an ionic radius of 0.111 nm, respectively, suggests that the formation of a solid solution through a substitutional mechanism is highly unlikely. Therefore, this leaves only one possibility, which is interstitial solid solubility of the rare earth cations (RECs) in the MnO$_2$ structure. The latter theory can be rationalized according to the types of MnO$_2$ crystal structures, which are schematically illustrated in Figure 1b. δ-MnO$_2$ has a 2D layered structure $(1 \times \infty)$ with an interlayer separation of ≈7 Å.[48,49] Such a large interlayer gap can easily accommodate the large-size RECs with partial phase transformation and minimal distortion.[50] The RECs can also stabilize the $(1 \times \infty)$ tunnels and thus shift the phase into the α/β-MnO$_2$ forms. In addition, α-MnO$_2$ provides atomic tunnels along the [001] direction (c-axis)[51] with lateral dimensions of 2×2 $(4.6 \times 4.6$ Å) and 1×1 $(1.9 \times 1.9$ Å).[52] The atomic tunnels along the [1$\bar{1}$0] direction of β-MnO$_2$ possess lateral dimensions of 3.4×3.4 Å. Therefore, similar to δ-MnO$_2$, the interstitial introduction of RECs is likely to occur in α/β-MnO$_2$ during crystallization, as has previously been reported.[53] The interstitial solubility of REC in MnO$_2$ is also expected to form high concentrations of structural defects.

To investigate the chemistry of structural defects that originate from unpaired electrons, electron paramagnetic resonance (EPR) analysis was conducted. The resultant spectra for pristine MnO$_{2-x}$ and $Mn_{1-x-y}(Ce_xLa_y)O_{2-\delta}$ are shown in Figure 1c. As for Mn ions, Mn^{2+} (3d^5, S = 5/2) and Mn^{4+} (3d^3, S = 3/2) species are EPR active, while Mn^{3+} (3d^4, S = 2), with no unpaired electrons, is EPR inactive. For pristine MnO$_{2-x}$, the EPR signal reveals a single broad line of Gaussian-like shape with a broad linewidth ($\Delta H_B = 367$ mT) owing to the dipole-dipole exchange
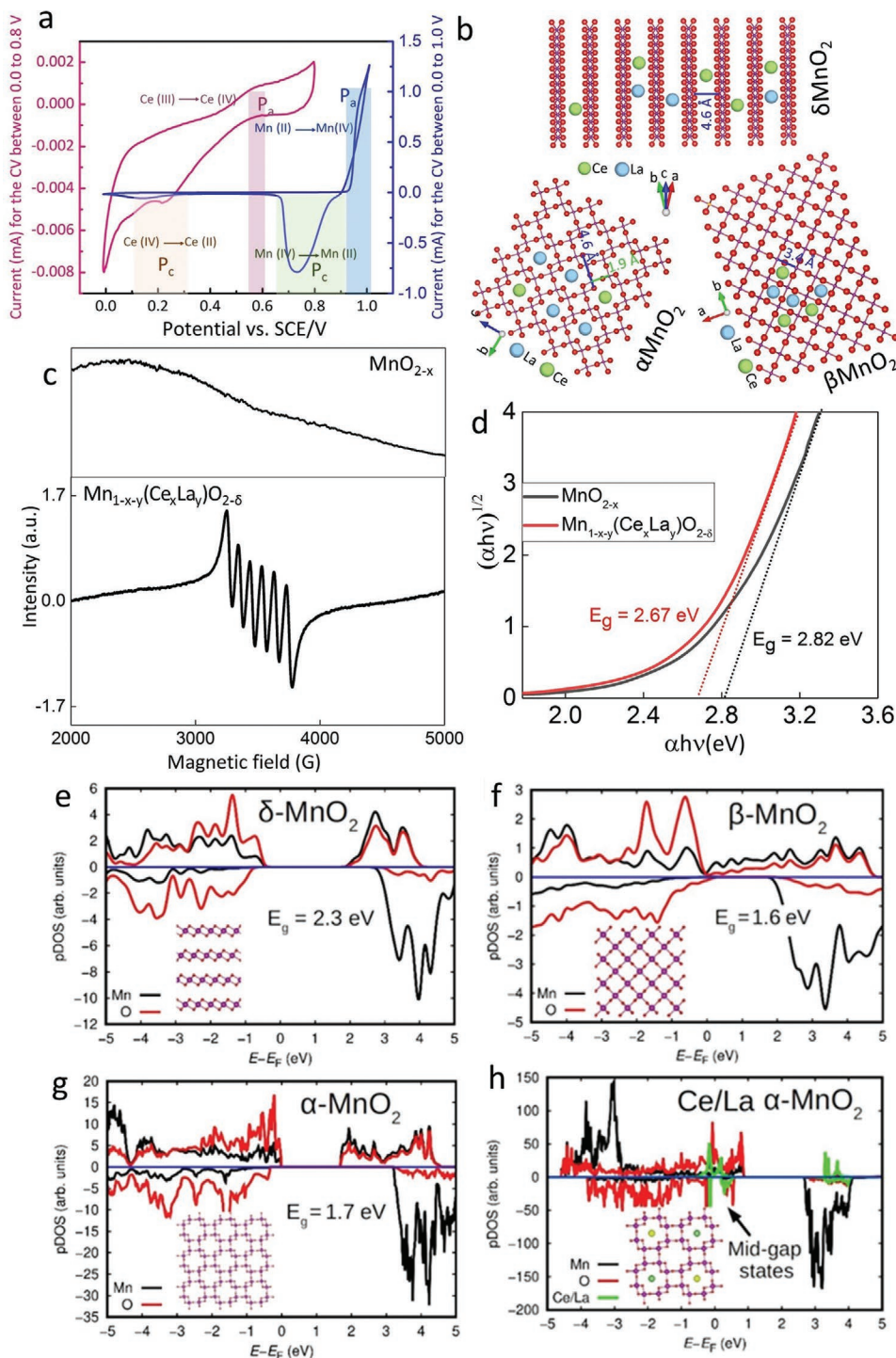
Figure 1. a) CVs of the precursor using a three-electrode configuration with FTO electrode as working electrode (WE), spiral Pt wire as the counter electrode (CE), and standard calomel electrode (SCE) as reference electrode (RE), at 10 mV s^{-1} scan rate and 70 °C, b) crystal structure of δ-, α-, and β-MnO$_2$ loaded with La^{3+} and Ce$^{3+/4+}$, c) EPR signals versus magnetic field curve of MnO$_{2-x}$ and Mn$_{1-x-y}$(Ce$_x$La$_y$)O$_{2-\delta}$ samples, and d) Tauc plot (UV–visible (αhν)$^{1/2}$ vs E$_P$ curve) for pristine MnO$_{2-x}$ and Mn$_{1-x-y}$(Ce$_x$La$_y$)O$_{2-\delta}$ powder samples; e–h) theoretical estimation of the electronic band properties of the (e) δ, (f) β, (g) α polymorphs of MnO$_2$, and (h) Mn$_{1-x-y}$(Ce$_x$La$_y$)O$_{2-\delta}$ based on first-principles DFT calculations. The bandgaps of the three polymorphs are different, with δ-MnO$_2$ presenting the largest value. The presence of Ce/La interstitial atoms induces the appearance of electronic mid-gap states. Mn, O, Ce, and La atoms are represented with violet, red, green, and yellow spheres, respectively.

interactions between two identical paramagnetic Mn^{4+} ions. The g factor of the signal was measured to be 1.96±0.01, which is consistent with those reported for MnO$_2$ nanostructures. For the Mn$_{1-x-y}$(Ce$_x$La$_y$)O$_{2-\delta}$ film, the corresponding EPR signal

ADVANCED
SCIENCE NEWS
www.advancedsciencenews.com

ADVANCED
FUNCTIONAL
MATERIALS
www.afm-journal.de

shows multiple hyperfine splitting at magnetic fields in the range of 320–380 mT that can be ascribed to the interactions between Mn^{2+}, Ce^{3+}, and La^{3+}. The co-existence of Mn^{4+} and Mn^{2+} for MnO and MnO_2 is manifested in the form of sharp hyperfine features, with g values[54] of 2.16, 2.10, and 1.96, with shoulders (rounded humps) on each hyperfine, respectively. The presence of Mn^{2+} is further justified by revealing the hyperfine feature with a g value of 2.005 associated with the Mn_3O_4 (2MnO MnO_2) phase in the system.[55] It is significant to note that the hyperfine interaction between unpaired electrons and atom nuclei yields information regarding the identity of ions and their distances. Ce posses four stable isotopes (^{136}Ce, ^{138}Ce, ^{140}Ce, and ^{142}Ce) and two oxidation states, 3+ and 4+, with respective electron configurations of $4f^{1}$ and $5p^{6}$. Despite the filled d orbital with the potential of forming ten absorption peaks, Ce^{4+} has no unpaired electrons and consequently is EPR-inactive. In contrast, Ce^{3+} has a single unpaired electron. Table S2, Supporting Information, provides g factors obtained according to the hyperfine interactions. As for the Ce dopant, the presence of Ce^{3+}, O_2^{-}, and Ce^{3+}–O^{-}–Ce^{4+} were identified as shown in Figure 1c. The hyperfine feature positioned at $g = 2.016$ indicates the existence of superficial isolated anionic vacancies caused by superoxide ligands linking to coordination Ce^{4+} ions.[54] In addition, the hyperfine feature with a g value of 1.96 can be assigned to a Ce^{3+}-$V_{\ddot{O}}$-Ce^{4+} interaction as a reflection of anionic vacancies on the surface.

Interstitial diffusion of Ce and La cations into the lattice structure can potentially modify the physical and chemical properties of functional materials, by controlling their ionic and electronic conductivities.[56] The atomic insertion into the MnO_{2-x} crystal structure in the form of cation intercalation can change the bonding energy. This is achieved by producing new molecular orbits which introduce impurity levels in semiconductors that can reduce the bandgap of the material.[57] The bandgap was evaluated using UV–vis absorption spectroscopy for $Mn_{1-x-y}(Ce_xLa_y)O_{2-\delta}$ and pristine MnO_{2-x} film electrodes, with similar thicknesses. Tauc plots in Figure 1d show that the bandgap shortened from 2.82 to 2.67 eV as a result of Ce and La co-insertion. Accordingly, the concentration of free movable electrons increases, which enhances electric conductivity. The substantial point defects and oxygen vacancies in the structure of MnO_{2-x} can also contribute to the improvement of electric conductivity.[50] This enhancement in electrical conductivity resulting from bandgap tuning and oxygen vacancies will in principle further improve the electrochemical performance, which is normally limited by carrier concentration and mobility.[57]

By using first-principles methods based on density functional theory (DFT), we estimated the electronic band properties of the α, β, and δ polymorphs of MnO_2 as well as the $Mn_{1-x-y}(Ce_xLa_y)O_{2-\delta}$ phase. The DFT results shown in Figure 1e indicates that i) the bandgap of the three undoped polymorphs are different, with δ-MnO_2 presenting the largest value ($E_g\approx2.3$ eV), and ii) Upon Ce/La insertion, the bandgap of MnO_2 can be further altered due to the appearance of electronic mid-gap states introduced by the interstitial metal ions. It is noted that the agreement between the theoretical and experimental E_g results is quantitatively not perfect for MnO_2 polymorphs. Such discrepancies, however, are understood based on the fact that in the DFT simulations, the analyzed systems are perfectly stoichiometric, whereas in the actual samples different types of defects are abundant (e.g., oxygen vacancies, which are known to affect E_g significantly). Nevertheless, at the qualitative level, the DFT simulations can be expected to be correct. Therefore, according to the DFT theoretical calculations, we may argue that the physical origins of the observed MnO_2 bandgap reduction induced by Ce/La insertion is twofold, namely, 1) the accompanying structural phase transformation from the δ to the α and β polymorphs, and 2) the appearance of Ce/La electronic mid-gap states. Similar to previous reports on ultrathin oxide materials,[58] the presence of midgap states and a reduced bandgap indicate enhanced electrical conductivity of the $Mn_{1-x-y}(Ce_xLa_y)O_{2-\delta}$ over pristine MnO_2.

The actual resistivity of MnO_2 and $Mn_{1-x-y}(Ce_xLa_y)O_{2-\delta}$ ultrathin films was measured using the four-point probe technique. The results match well with those obtained qualitatively revealing an ≈11% reduction of resistivity upon insertion of Ce/La cations in the $Mn_{1-x-y}(Ce_xLa_y)O_{2-\delta}$ ultrathin films, as shown in Figure S4, Supporting Information.

2.2. Optical and Chemical Analysis of Transparent Ultrathin Films

The flexibility of the anodic chronoamperometric synthesis allows for the fabrication of ultrathin films with tailored thicknesses and thereby transparency. **Figure 2**a shows digital images of $Mn_{1-x-y}(Ce_xLa_y)O_{2-\delta}$ ultrathin films where the film thickness increases from left to right as evident by the diminution of their transparencies. The morphological alteration of the ultrathin films as a function of deposition time was explored using field-emission scanning electron microscopy (FE-SEM) images, as shown in Figure 2b. The sequential FE-SEM images reveal that ultrathin films are deposited through stacking of the extremely thin nanoflakes across the surface of the fluorine-doped tin oxide (FTO) substrate.

The $Mn_{1-x-y}(Ce_xLa_y)O_{2-\delta}$ films exhibited 2D nanosheet-like morphology, which remained unchanged by increasing the thickness and the interstitial introduction of Ce and La. The ultrathin Mn-oxide-based nanosheets have been previously shown to deliver a high exposed surface area that is critical for achieving high energy density. It has been shown[59] that flake-like microstructure of the Mn oxides enhances the faradic reactions between the active material (in electrode) and the electrolyte, thereby enhancing the specific capacitance of the supercapacitor. Furthermore, considering the XPS results which show high concentrations of point defects, owing to the presence of low Mn oxidation states (Mn^{2+} and Mn^{3+}), this type of morphology is highly advantageous since it maximizes the exposure of the structural defects and thus enhances the electrochemical performance, which is directly influenced by the number of these defects.

Figure 2c shows the transmittance spectrum obtained for each film within a wide range between 300 and 900 nm. The relationship between the optical transmittance (T%) of the films, at 550 nm, and thicknesses is plotted, as shown in Figure 2d. The results show that for thicknesses ≤46 nm (samples II, III, IV), an outstanding T% value of >≈90% can be achieved.
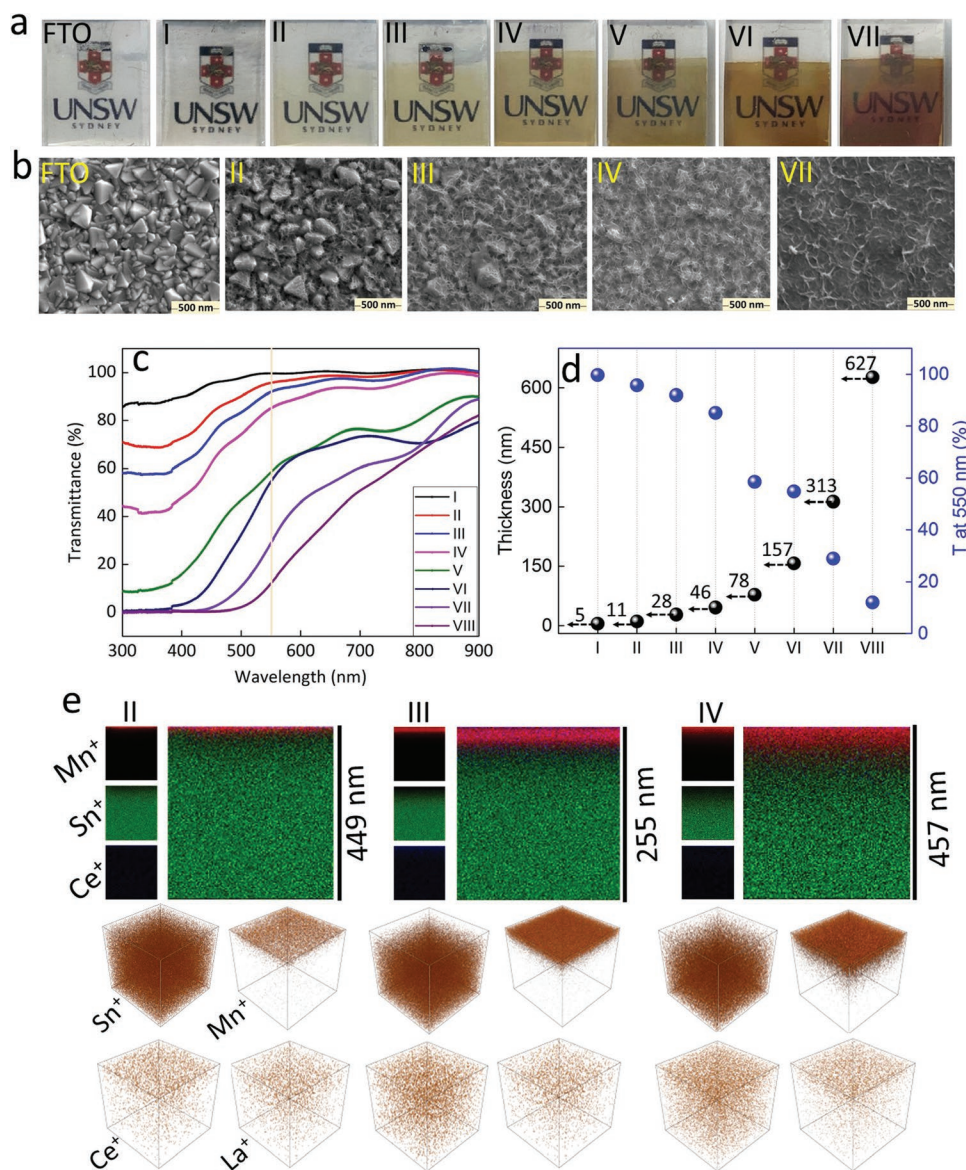
Figure 2. a) Optical images of the as-synthesized $Mn_{1-x-y}(Ce_xLa_y)O_{2-\delta}$ thin-film electrodes, b) FE-SEM images of the surface of selected samples presented in (a), c) UV–vis transmittance spectra of the corresponding films in the visible region, d) transmittance of the films at the wavelength of 550 nm as a function of thickness; and e) 2D and 3D TOF-SIMS elemental images for the measurement of the thickness, qualitative concentration, and distribution of elements in the as-synthesized films.

However, increasing the thickness to 78 nm (sample V) results in a considerable T% reduction to <60%. Furthermore, an increase in thickness to 627 nm yields a low T% value of 12% (sample VIII). Table S3, Supporting Information, summarizes the physical and optical properties of the ultrathin films.

To measure the thickness of the films, TOF-SIMS analysis was used. The results of 2D TOF-SIMS analysis for three representative samples II, III, and IV are shown in Figure 2e. According to the penetration depth of the ion beam, the thickness of the films was measured to be 11, 28, and 46 nm for samples II, III, and IV, respectively. Figure 2e shows the bulk distribution of Mn, Ce, and La ions for the three representative samples II, III, and IV, revealing a homogenous distribution of the ions across the ultrathin films.

In order to confirm the accuracy of the TOF-SIMS results in this study, an additional TEM analysis on the optimum $Mn_{1-x-y}(Ce_xLa_y)O_{2-\delta}$ ultrathin film with a thickness of 46 nm (measured by TOF-SIMS) was carried out and compared. The TEM image is provided in Figure S5, Supporting Information.

2.3. Electrochemical Performance of Ultrathin Films

The electrochemical behavior of the $Mn_{1-x-y}(Ce_xLa_y)O_{2-\delta}$ ultrathin films was investigated in a three-electrode configuration system in a 2 M KOH electrolyte. **Figure 3**a,b shows CVs of the films at scan rates of 5 and 50 mV s^{-1} within the potential window of −0.3 to 0.5 V versus SCE. The peak areas
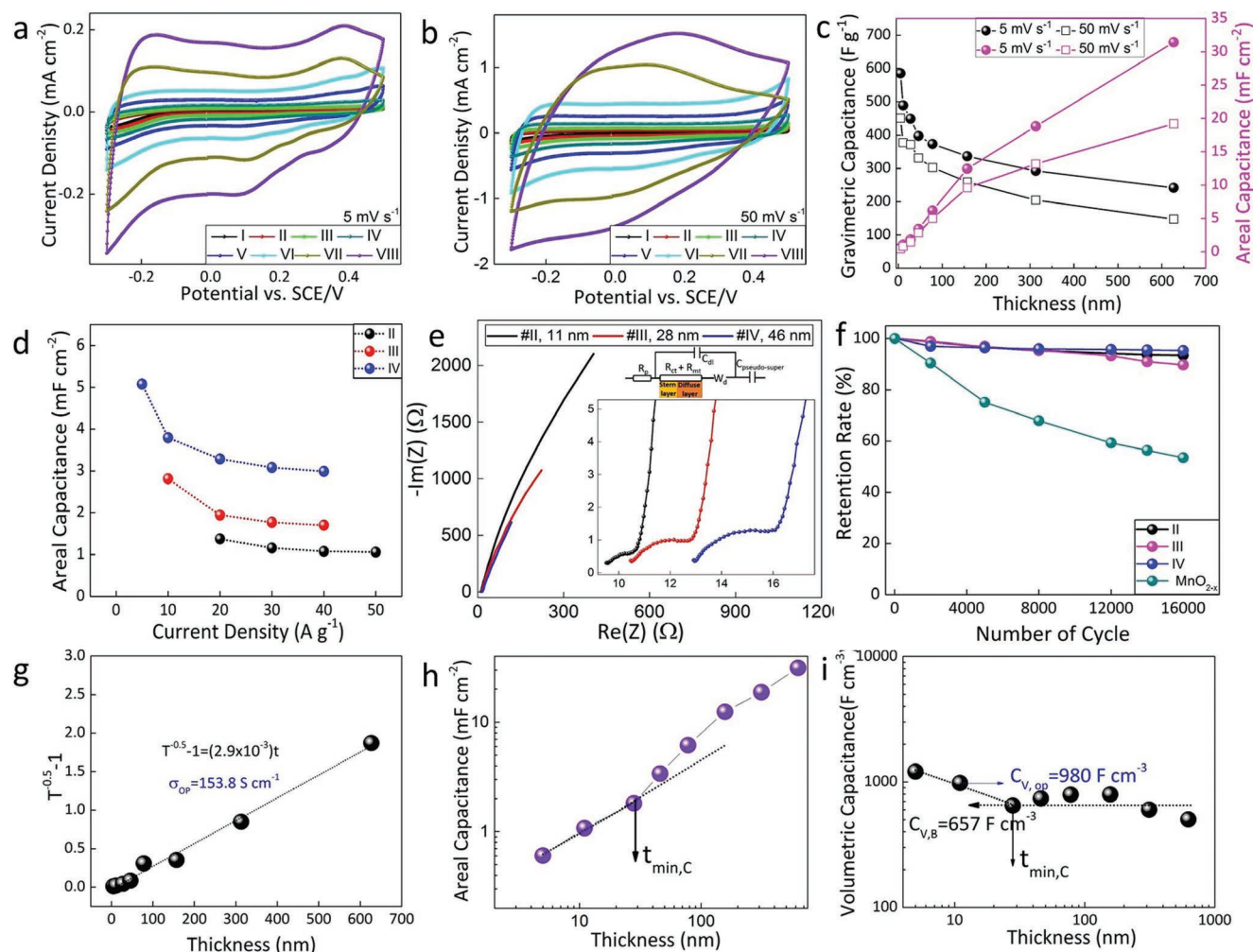
Figure 3. Electrochemical results of the as-synthesized $Mn_{1-A}Ce_xLa_yO_{2-B}$ thin-film electrodes using a three-electrode cell configuration (thin-film electrode as WE, Pt spiral wire as CE, and SCE as RE) in the potential window from −0.3 to 0.5 versus SCE/V in a 2 M KOH aqueous solution. CV of electrodes at scan rates of a) 5 mV s^{-1}, and b) 50 mV s^{-1}; c) areal and gravimetric capacitances as a function of film thickness; d) areal capacitance as a function of scan rate for the three thinnest electrodes II, III, and IV based on GCD test; e) EIS for the synthesized electrodes at 0.0 versus SCE/V between 100 kHz to 100 mHz with the potential amplitude of 10 mV; f) stability performance of the three $Mn_{1-x-y}(Ce_xLa_y)O_{2-\delta}$ electrodes #II (at 35 A g^{-1}), #III (at 20 A g^{-1}), and #IV (at 15 A g^{-1}), and pristine MnO_{2-x} film (at 15 A g^{-1}). g–i) The impact of percolation and thickness on the optoelectronic properties of ultrathin films; (g) plot of film transmittance expressed as $T^{-0.5}-1$ as a function of film thickness, (h) areal capacitance, and (i) volumetric capacitance of the films as a function of film thickness, using CV results at a scan rate of 5 mV s^{-1} in a 2 M KOH electrolyte.

of the voltammograms, which are associated with the areal capacitance (F cm^{-2}) of the films, are shown to be enhanced by increasing the film thickness. The difference in the CV shapes obtained at 5 and 50 mV s^{-1} is ascribed to the alteration of charge/discharge mechanism and the depletion of charge carriers as a result of the rapid kinetics of the charge/discharge process. It is critical to note that the insignificant contribution of the substrate for the thinnest film, that is, 11 nm, # II, was measured to be only ≈3%, as shown in Figure S6c, Supporting Information. Further analysis of the electrochemical behavior of the films was carried out using CV over a wide range of scan rates. The details of the results are shown in Figure S7a–c, Supporting Information. Furthermore, a comparative plot of areal and gravimetric capacitances against the films' thicknesses, at two scan rates of 5 and 50 mV s^{-1}, is shown in Figure 3c.

The results reveal that increasing the film thickness from 11 to 627 nm reduced the gravimetric capacitance by 53%, while the areal capacitance increased from ≈0.1 to 32.0 mF cm^{-2}. The apparent capacitance gap between the scan rates originates from the contribution of diffusion, which becomes insignificant at a rapid scan rate of 50 mV s^{-1}.

To confirm the results of capacitance obtained by CV, the galvanostatic charge/discharge (GCD) technique was used. Figure 3d shows a plot of areal capacitance against current density, which is consistent with those obtained from the CV technique. The other gravimetric and areal capacitances of the ultrathin films at different scan rates and current densities are illustrated in Figure S7g–i, Supporting Information, respectively.

Electrochemical impedance spectroscopy (EIS) of the films, recorded at open circuit potential (OCP) with a potential

**ADVANCED
SCIENCE NEWS**

www.advancedsciencenews.com

**ADVANCED
FUNCTIONAL
MATERIALS**

www.afm-journal.de

amplitude of 10 mV, is shown in Figure 3e. To analyze the EIS measurements, a physicochemical transport model was applied (shown in the inset of Figure 3e), where the electrode resistance (R_p) is obtained by summation of resistances in the bulk electrode and at the interface between the electrode and current collector.[60] The R_p values for the combination of FTO substrate and films #II, #III, and #IV were measured to be ≈9.5, 10.5, and 13.0 Ω, respectively. The calculated results for the $Mn_{1-x-y}(Ce_xLa_y)O_{2-\delta}$ film indicate that with ≈17 nm increase in the thickness, the resistance escalates by 1.0–1.5 Ω. Furthermore, the sum of the charge and mass transfer resistance ($R_{ct} + R_{mt}$) was measured to be ≈0.29, 0.65, and 0.94 Ω for films #II, #III, and #IV, respectively. The transition from medium (semicircle) to low frequencies (linear line), which is represented by a Warburg diffusion element (W_d), describes the diffusion of ions in the electrolyte.[61] The slope of the line, at low frequencies, indicates whether the charging is under EDL formation (>45°) or limited by ion diffusion in the electrolyte (<45°).[60] The general sharp slopes achieved for all the samples indicates the presence of the EDL layer and predominant contribution of pseudocapacitance.[61]

The capacitance retention of the $Mn_{1-x-y}(Ce_xLa_y)O_{2-\delta}$ films #II, #III, and #IV, and pristine MnO_{2-x} film (with the thickness equal to #IV, i.e., 46 nm) were investigated using GCD analysis at current densities of 35, 20, and 15 A cm^{-1}, respectively. Figure 3f shows excellent electrochemical stability with 95, 90, and 93% capacitance retention for films #II, #III, and #IV, respectively, after 16 000 charge/discharge cycles. Such outstanding performance stability can be associated with the presence of the RECs that are shown to enhance the structural and corrosive stabilities.[62] In contrast, the pristine MnO_{2-x} film suffers from rapid degradation while cycling.

To obtain an optimal transparent pseudocapacitor, establishing an equilibrium between the specific capacitance, which is either gravimetric or areal, and optoelectronic properties is critical. In the present work, ultrathin film #II, with a thickness of 11 nm, exhibited a relatively low areal capacitance of 1.37 mF cm^{-2}, but the highest transparency (96%) (Figure 2c). The increase in thickness to 28 (sample #III) and 46 nm (sample #IV) resulted in enhancement of the areal capacitance to 2.81 and 5.07 mF cm^{-2}; however, reduced the gravimetric capacitance from 720 to 622 F g^{-1} while limiting the transparency to 92 and 85%, respectively. Although transparency can be achieved via the fabrication of ultrathin electrodes, minimizing the thickness to increase the transparency (Figure 2c) can introduce certain limitations due to percolation pathways, below which the obtained transparency is not efficient for energy storage applications.

As a matter of fact, the intrinsic properties, including optoelectronic properties, are thickness independent[63] only in bulk-like materials.[64] Therefore, the transition from bulk-like to percolative regimes, that is, ultrathin thicknesses, and percolation impact in ultrathin films, should be taken into account.[65] This is because when the thickness falls below the transition thickness, the percolative impact begins to control the optoelectrical conductivity.[14,66,67] Besides, while volumetric capacitance is thickness invariant for thick films, a significant deviation from the bulk-like behavior was observed for ultrathin films.

To demonstrate the presence of both bulk-like and percolative regimes, a further investigation was carried out, where the impact of thickness on the optoelectronic properties of ultrathin films was analyzed. For conductive films, the transmittance (T) for a given thickness, t, is controlled by the optical conductivity (σ_{op}) through Equation (1):[4,19,64]

$$T = \left[1 + \frac{Z_0 \sigma_{op} t}{2}\right]^{-2} \tag{1}$$

where z_0 is the impedance of free space (377 Ω). Therefore, the optical conductivity (σ_{op}) was calculated to be σ_{op} = 153.8 S cm^{-1} by measuring the slope of the line in the plot of $T^{-1/2}-1$ (at 550 nm) against the thickness of the film (t), as shown in Figure 3g. This value is the lowest reported to date for transparent supercapacitors such as SWCNT films (σ_{op} = 150–200 S cm^{-1})[68,69] and graphene films (σ_{op} = 100–2000 S cm^{-1}).[70]

The areal capacitances that were calculated based on the CV curves are plotted against the film's thickness in Figure 3h. As shown, for thin films with thicknesses below 28 nm, the areal capacitance varies linearly with thickness. It is reasonable to consider this thickness value as the transition thickness ($t_{min,C}$ = 28 nm) around which the regime varies from percolative to bulk-like behavior.

To further confirm this outcome, the film thickness was used to calculate the volumetric capacitance, which is plotted as a function of thickness as shown in Figure 3i. Considering that the as-synthesized film possesses a well-defined surface area per unit volume, then this volumetric capacitance (C_V) should be independent of the film's thickness for a bulk-like film (assuming good electrolyte wetting). In the bulk-like regime ($t_{min,C}$>28 nm), as expected, C_V is relatively constant with a small variation around a mean value of 657 F cm^{-3}. In contrast, in the percolative region ($t_{min,C}$<28 nm), a significant increase in C_V value is observed, which is attributed to the lower thickness, which facilitates and expedites the movement of the electrons towards the current collector substrate which therefore results in higher capacitance.

While the thicknesses can be reduced to increase transmittance, the areal capacitance decreases (Figure 3h). Therefore with a trade-off between transmittance and capacitance and in order to optimize the areal capacitance (C_A) at certain transparency, the "capacitive figure of merit" (FoM$_c$), C_V/σ_{op}, should be maximized.[64] The FoM$_c$ is determined to be C_V/σ_{op} = 7.8, 6.3, and 4.2 F S^{-1} for electrodes II, III, and IV, respectively. The values obtained in the present work are amongst the highest reported to date including a RuO$_2$/PEDOT:PSS thin film (C_V/σ_{op} = 6.1 F S^{-1}),[4] PEDOT:PSS (C_V/σ_{op} = 1.7 F S^{-1}),[64] and a disordered SWNT electrode (C_V/σ_{op} = 0.3 F S^{-1}).[19]

2.4. Impact of RECs in $Mn_{1-x-y}(Ce_xLa_y)O_{2-\delta}$ Lattice on Energy Storage and Cycling Stability

2.4.1. Energy Storage Mechanism

There are two principal mechanisms during charge/discharge of the $Mn_{1-x-y}(Ce_xLa_y)O_{2-\delta}$ film: i) redox reactions at the surface of the electrode, which is the characteristic of pseudocapacitance[71–73] and ii) intercalation/de-intercalation of the cations, which is characteristic of
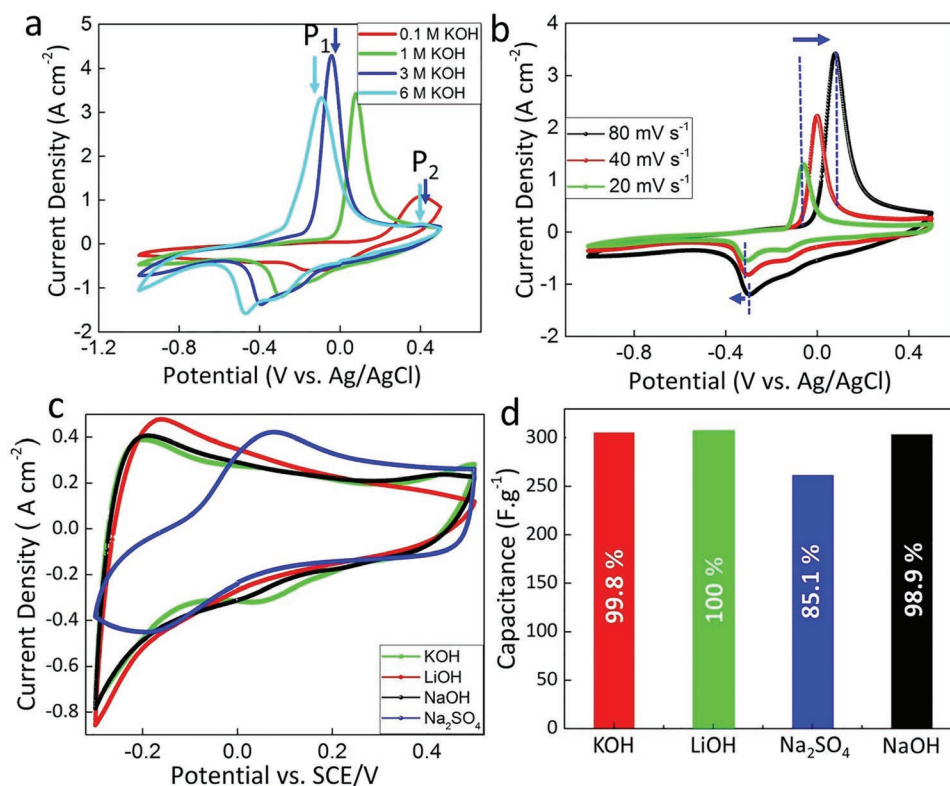
Figure 4. Effect of electrolyte concentration on redox reactions and intercalation mechanism of ions, using an electrode made of #IV ultrathin film; a) CVs at the scan rate of 80 mV s^{-1} in aqueous KOH electrolytes of varying concentration, b) CVs at 1 M KOH electrolyte at different scan rates, c) CVs at electrolyte with charge carrier cations of 2 M Li$^+$, Na$^+$, K$^+$, and neutral electrolyte of SO$_4^{2-}$ (using Na$_2$SO$_4$), and d) corresponding gravimetric capacitance.

intercalation pseudocapacitance.[74,75] The former mechanism is determined by the number of active sites, for example, vacancies, at the surface of the electrode, while the latter mechanism requires crystallographic pathways that allow the charge carriers to intercalate/de-intercalate within/out of the bulk of the electrode.

To elucidate the intercalation/de-intercalation mechanism, alterations in the voltammogram shapes in response to the increasing pH of the electrolyte (i.e., increasing hydroxyl ion (OH$^-$) concentration) were investigated and hence the resultant CVs are shown in **Figure 4**a. With the increase of the OH$^-$ concentration, the peak potentials for both reduction and oxidation reactions shifted to lower values which clarify the key role of OH$^-$ ions during the charge/discharge process. During the anodic scan, the voltammogram exhibits two distinctive peaks related to two oxidation reactions of Mn^{2+} → Mn^{3+} and Mn^{3+} → Mn^{4+}. It is significant to note that the former oxidation reaction shows greater intensity implying a higher concentration of Mn^{2+}, which is consistent with the results of EPR analysis (Figure 1c). The large concentration of OH$^-$, and thus its high accessibility, in the electrolyte would result in the dissociation of OH$^-$ to O^{2-} during the anodic scan.[76] This can be followed by intercalation of the liberated O^{2-} into the vacancy sites and atomic gaps within the 2D layered structure (1 × ∞) of δ-MnO$_2$ of the Mn$_{1-x-y}$(Ce$_x$La$_y$)O$_{2-\delta}$ electrode, which is more likely in comparison to that of H$^+$ with negligible concentration.[77] The charge/discharge process through O^{2-} intercalation/de-intercalation is advantageous since it delivers two charges, rather than the

typical single charge carriers. Therefore, a notable enhancement in the specific capacitance is expected.[78] The free O^{2-} intercalates into the vacancy sites, which is then accompanied by proton transfer to the electrolyte hydroxide ions yielding water as a product.[76] At a very low OH$^-$ concentration (0.1 M), shown in Figure 4a, the peak associated with the Mn^{3+} → Mn^{4+} reaction is significantly decreased confirming the significant role of OH$^-$ concentration in O^{2-} anion intercalation.

Owing to the large ionic radius of O^{2-}, the intercalation is anticipated to be kinetically slow and hence diffusion-controlled. This is supported by voltammograms obtained at scan rates of 20, 40, and 80 mV s^{-1} (Figure 4b). The increase in the scan rate resulted in a shift of the anodic peaks to higher potential that can be attributed to the sluggish kinetics of O^{2-} intercalation within the insufficient scanning time. In contrast, for the cathodic cycle, increasing the scan rate resulted in an insignificant shift in the cathodic peak potentials. This is owing to the fact that, during the cathodic cycle, restoration of the vacancies occurs by breaking the chemical bonds between the intercalated O^{2-} and coordinated Mn atoms. Therefore, de-intercalation of the as-released O^{2-} would not affect the peak potentials by increasing the scan rate.

To further confirm that O^{2-} intercalation has a substantial contribution to the energy storage performance of the Mn$_{1-x-y}$(Ce$_x$La$_y$)O$_{2-\delta}$, Figure 4c shows CVs of Mn$_{1-x-y}$(Ce$_x$La$_y$)O$_{2-\delta}$ obtained in basic electrolytes with Li$^+$, Na$^+$, K$^+$ charge carriers and a neutral electrolyte of 2 M Na$_2$SO$_4$. The measurement of voltammogram areas (Figure 4d) revealed that

the capacitances obtained in basic electrolytes exhibited ≈15% increase compared to the ones obtained in neutral electrolytes. Furthermore, the type of charge carriers in basic electrolytes showed no significant impact on the capacitance indicating that cations are not involved in the intercalation process.

Another critical factor in controlling the rate of intercalation/de-intercalation of O^{2-} is the density of Mn cations, with lower oxidation states, and probably oxygen vacancies, which act as active sites to entrap the O^{2-} species. The presence of these active sites has been shown to change the electronic conductivity of the $Mn_{1-x-y}(Ce_xLa_y)O_{2-\delta}$ by realignment of the band positions, possibly through an introduction of midgap states.[77] Additionally, the formation of midgap states can also be attributed to the presence of La^{3+} and Ce^{3+} ions. The Tauc plot shown in Figure 1d unveiled such an alteration, relative to the pristine MnO_{2-x}. Furthermore, the multivalence charge transfer (MVCT) between the RE and Mn ions significantly impacts the electrochemical performance by improving the electrical conductivity.[50,79,80] Another reason for the improved electrochemical performance of the $Mn_{1-x-y}(Ce_xLa_y)O_{2-\delta}$ is the formation of tensile distortion, owing to the presence of RE ions at the interstitial sites of the lattice, thus enabling ion transport by newly established atomic channels.[12,81]

Owing to the different valance charges of Mn ions, cooperative Jahn–Teller effect (CJTE) is another factor that could impact the conductivity of the $Mn_{1-x-y}(Ce_xLa_y)O_{2-\delta}$ samples. Mn^{4+} ions are not Jahn–Teller (JT) active; however, the presence of Mn^{3+} ions in $Mn_{1-x-y}(Ce_xLa_y)O_{2-\delta}$ structure offers a large CJTE, where the lattice distortion originates from individual JT centers in complex compounds.[82–84] The displacement of a portion of La/Ce ions in long-ranged $Ce/La-O-Mn^{3+}-O-Ce/La$ interactions in distorted octahedral sites can be periodically distorted in Mn stripes using a charge modulation. Since in the structure of $Mn_{1-x-y}(Ce_xLa_y)O_{2-\delta}$ there are not enough Ce/La ions to form linear 180° $Ce/La-O-Mn^{3+}-O-La-Ce$ configuration, Ce/La ions relax to disordered octahedral sites instead of the formation of $V_{La/Ce}-O-Mn^{3+}-O-Ce/La$. In the octahedral sites, the Ce/La ions share the symmetric attraction of two adjacent JT-disordered $-O-Mn^{3+}-O-Ce-La$ configurations. As the linear 180° configuration is not stable,[82] a long-ranged $V_{La/Ce}-Ce/La$ repulsion in JT centers is produced through Mn charge and d-orbital orderings.

2.4.2. Impact of RECs Insertion on Cyclic Stability

Comparative analyses were carried out to explore the chemical alterations of MnO_{2-x} and $Mn_{1-x-y}(Ce_xLa_y)O_{2-\delta}$ electrodes during charge/discharge cycling. Therefore, variations in defect concentrations, as a reflection of Mn oxidation states, before and after charge/discharge of the 1st and 16 000th cycles for pristine MnO_{2-x} and $Mn_{1-x-y}(Ce_xLa_y)O_{2-\delta}$ were examined using XPS analysis, the results of which are shown in **Figure 5**. Figure 5a,b show XPS spectra for Mn $2p_{3/2}$ orbital of pristine MnO_{2-x} and $Mn_{1-x-y}(Ce_xLa_y)O_{2-\delta}$. The spectra are deconvoluted into four distinctive multiplets using a Gaussian fitting technique. The multiplets positioned at 641.1, 642.2, and 643.5 eV are assigned to Mn^{2+}, Mn^{3+}, and Mn^{4+}, respectively.

The atomic concentrations of the Mn oxidation states for the as-synthesized MnO_{2-x}, fully-discharged MnO_{2-x} after one cycle,
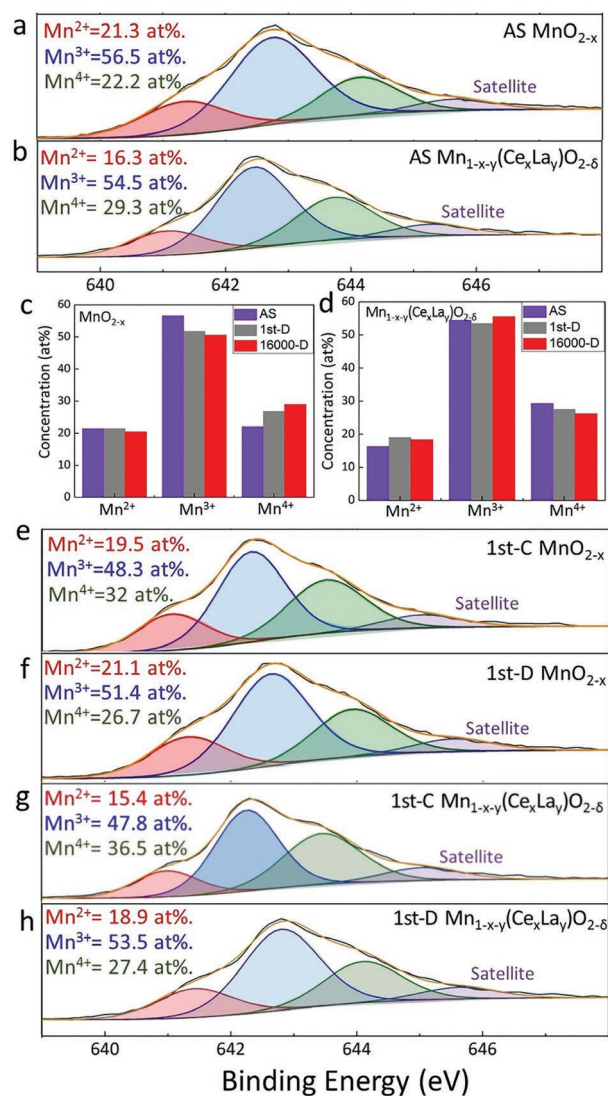

Figure 5. XPS spectra associated with the Mn $2p_{3/2}$ of a) pristine MnO_{2-x}, b) $Mn_{1-x-y}(Ce_xLa_y)O_{2-\delta}$. Alteration of Mn oxidation state, discharge (D) of 1st and 16 000th cycles for c) pristine MnO_{2-x}, and d) $Mn_{1-x-y}(Ce_xLa_y)O_{2-\delta}$, (AS stands for as-synthesized). XPS spectra associated with the Mn $2p_{3/2}$ of pristine MnO_{2-x} showing the concentration of Mn^{2+}, Mn^{3+}, Mn^{4+} during 1st cycle's e) charge (C), and f) discharge (D). XPS spectra associated with the Mn $2p_{3/2}$ of $Mn_{1-x-y}(Ce_xLa_y)O_{2-\delta}$ showing the concentration of Mn^{2+}, Mn^{3+}, Mn^{4+} during 1st cycle's g) charge (C), and h) discharge (D).

and fully-discharged MnO_{2-x} after 16 000 cycles are plotted in Figure 5c. The low Mn oxidation states (Mn^{2+} and Mn^{3+}), which are counted as active sites, where O^{2-} anions can be inserted, are crucial to enhance the capacitance. In contrast, the Mn^{4+}, which is obtained after the full-discharge process, is practically inactive for energy storage performance. In the present work, MnO_{2-x} exhibits typical behavior, similar to other TMOs reported previously, in that Mn^{2+} and Mn^{3+} concentrations decrease with cycling, while Mn^{4+} concentration shows an increasing trend. Therefore, the capacitance retention is expected to decrease with cycling. This has been confirmed by more than 40% capacitance reduction observed after 16 000 cycles.

**ADVANCED
SCIENCE NEWS**
www.advancedsciencenews.com

**ADVANCED
FUNCTIONAL
MATERIALS**
www.afm-journal.de

In contrast, the XPS results for $Mn_{1-x-y}(Ce_xLa_y)O_{2-\delta}$ sample, as shown in Figure 5d, revealed unprecedented behavior, where the atomic concentrations of Mn^{2+} and Mn^{3+} increased during the discharge process after 16 000 cycles. This is accompanied by a decrease of Mn^{4+} from 29.3 to 25 at%. These results rationalize the outstanding capacitance retention of $Mn_{1-x-y}(Ce_xLa_y)O_{2-\delta}$ yielding an insignificant capacitance reduction of ≈10% after 16 000 cycles.

A more comprehensive investigation was carried out by a comparative study on Mn concentrations for the charge and discharge process. For the as-synthesised MnO_{2-x} sample, the initial concentrations were measured to be 21.3, 56.5, and 22.2 at% for Mn^{2+}, Mn^{3+}, and Mn^{4+}, respectively (Figure 5a). The 1st cycle of charge resulted in oxidation of Mn^{2+} and Mn^{3+} toward Mn^{4+}. Therefore, the concentration of Mn^{2+} and Mn^{3+} decreased to 19.5 and 48.3 at%, while the Mn^{4+} concentration increased by 10 to 32 at% (Figure 5e). During the following discharge process, however, an incomplete restoration of Mn oxidation states occurred that caused a reduction of Mn^{2+} and Mn^{3+} concentrations, relative to the as-synthesized sample, which led to the evolution of Mn^{4+}. The resultant concentrations of Mn^{2+}, Mn^{3+}, and Mn^{4+} after the first cycle of discharge were measured to be 21.1, 51.4, and 26.7%, respectively (Figure 5f). The constant reduction of Mn^{2+} and Mn^{3+} during 16 000 charge/discharge cycles was observed, as shown in Figure 5f.

Figure 5b shows the as-synthesized $Mn_{1-x-y}(Ce_xLa_y)O_{2-\delta}$ possessing high densities of Mn with low oxidation states, that is, Mn^{2+} (16.3 at%) and Mn^{3+} (54.5 at%), and only 29.3 at% of Mn^{4+}. During the first cycle of charge, Mn^{2+} and Mn^{3+} are oxidized to Mn^{4+} leading to a drop in the Mn^{2+}/Mn^{3+} concentrations by ≈1 and 7%, respectively while the Mn^{4+} concentration increased to 36.5% (Figure 5g). Upon discharge (Figure 5h), not only were the Mn^{2+} and Mn^{3+} concentrations fully reversed, but also new Mn^{2+} states were generated. The concentrations of Mn^{2+}, Mn^{3+}, and Mn^{4+} were measured to be 18.9, 53.5, and 27.4%, respectively. A similar trend was observed after 16 000 cycles.

The microstructure of the pristine MnO_{2-x} and $Mn_{1-x-y}(Ce_xLa_y)O_{2-\delta}$ were examined after 2500 and 16 000 cycles, respectively, and the corresponding SEM images are shown in Figure S8a–d, Supporting Information. It clearly reveals the trend where nanoflakes in the as-synthesized pristine MnO_{2-x} transform to nanowires after 2500 cycles while the microstructure of $Mn_{1-x-y}(Ce_xLa_y)O_{2-\delta}$ remained unchanged even after 16 000 cycles. These results confirm that the REC interstitials play a critical role in retaining the microstructure and hence the energy storage performance.[81,85]

In summary, morphology, phase stability, and conductivity are three key factors induced by REC insertion resulting in promising pseudocapacitor electrodes with significantly enhanced performance stability.

2.5. Electrochemical Performance of a Flexible, Transparent, and Symmetric Pseudocapacitance Device

Capacitance values can significantly vary in different experimental setups even with identical materials.[86,87] The electrochemical performance of the $Mn_{1-x-y}(Ce_xLa_y)O_{2-\delta}$ ultrathin film with a thickness of 46 nm (#IV) was studied by

synthesis of a flexible symmetric pseudocapacitance device. The rationale to select sample #IV was for a fully combined study of transparency and areal, gravimetric, and volumetric capacitances. **Figure 6**a shows voltammograms obtained in a symmetric two-electrode ($Mn_{1-x-y}(Ce_xLa_y)O_{2-\delta}$ film coated on FTO) configuration system in a 2 M KOH aqueous solution at scan rates ranging from 5 to 1000 mV s^{-1} within the potential window of −0.3 and +0.5 V versus SCE. The clear rectangular shape of the voltammogram is an indication of the EDL and pseudocapacitance behavior. The gravimetric and areal capacitances of the electrode as a function of scan rate were plotted, as shown in Figure 6b. Both specific capacitances decrease by increasing the scan rate, similar to the three-electrode configuration system. According to the theory reported in the literature,[86] the specific capacitance obtained from the three-electrode system is calculated to be ca. quadruple that from the symmetric two-electrode system even with totally identical materials.[87] For instance, comparing the gravimetric capacitance (142 F g^{-1}) obtained from the two-electrode aqueous setup at a scan rate of 5 mV s^{-1} (Figure 6b) with the one (489 F g^{-1}) obtained from the three-electrode configuration (for #IV) under the same condition (Figure S7h, Supporting Information) indicates that in our work $C_{three-electrode} = 3.4 \times C_{two-electrode}$, showing that the two-electrode configuration is very close to what is expected based on theoretical calculations.

The quasi-triangle shape of the GCD profiles at various current densities is also shown in Figure S9a, Supporting Information. The areal and gravimetric capacitances in Figure 6c are in accordance with those obtained from the CV method (Figure 6b). Further comparison between the gravimetric capacitance values obtained using a two-electrode GCD test configuration (132 F g^{-1}) at a specific current of 10 A g^{-1} (Figure 6c) with one (466 F g^{-1}) obtained using a three-electrode configuration (for #IV at Figure S7i, Supporting Information) shows that $C_{three-electrode} = 3.5C_{two-electrode}$, which is consistent with the CV comparison and also close to the theoretical value. The cycling stability of the two-electrode system was evaluated using the GCD method (Figure 6d). The results show high capacitance retention of ≈82% after a large number of cycles (16 000) at a current density of 10 A g^{-1}.

The two-electrode configuration system was further analyzed using a device with a solid-state electrolyte (a gel mixed of LiCl, Polyvinylalcohol (PVA), and H_2O), which are superior, in terms of safety, compared to conventional liquid electrolytes.[88] Figure S9b, Supporting Information, shows the resultant CVs at scan rates in the range of 5–1000 mV s^{-1} and in the potential window from −0.3 to +0.5 V versus SCE.

The small deviation from the ideal-rectangular shape and lower current density can be attributed to the larger electrical resistance resulting from the slower electron transfer rate within the solid electrolyte. This is shown in Figure 6e, where the gravimetric and areal capacitances of the symmetric two-electrode device, as a function of scan rate in a solid electrolyte, experience a slight decrease compared with those obtained from a similar system but in an aqueous electrolyte. This indicates the excellent potential applicability of these $Mn_{1-x-y}(Ce_xLa_y)O_{2-\delta}$ ultrathin films as electrode materials in flexible and transparent pseudocapacitance devices.

The power and energy densities of the device were also measured and compared with the outstanding values reported
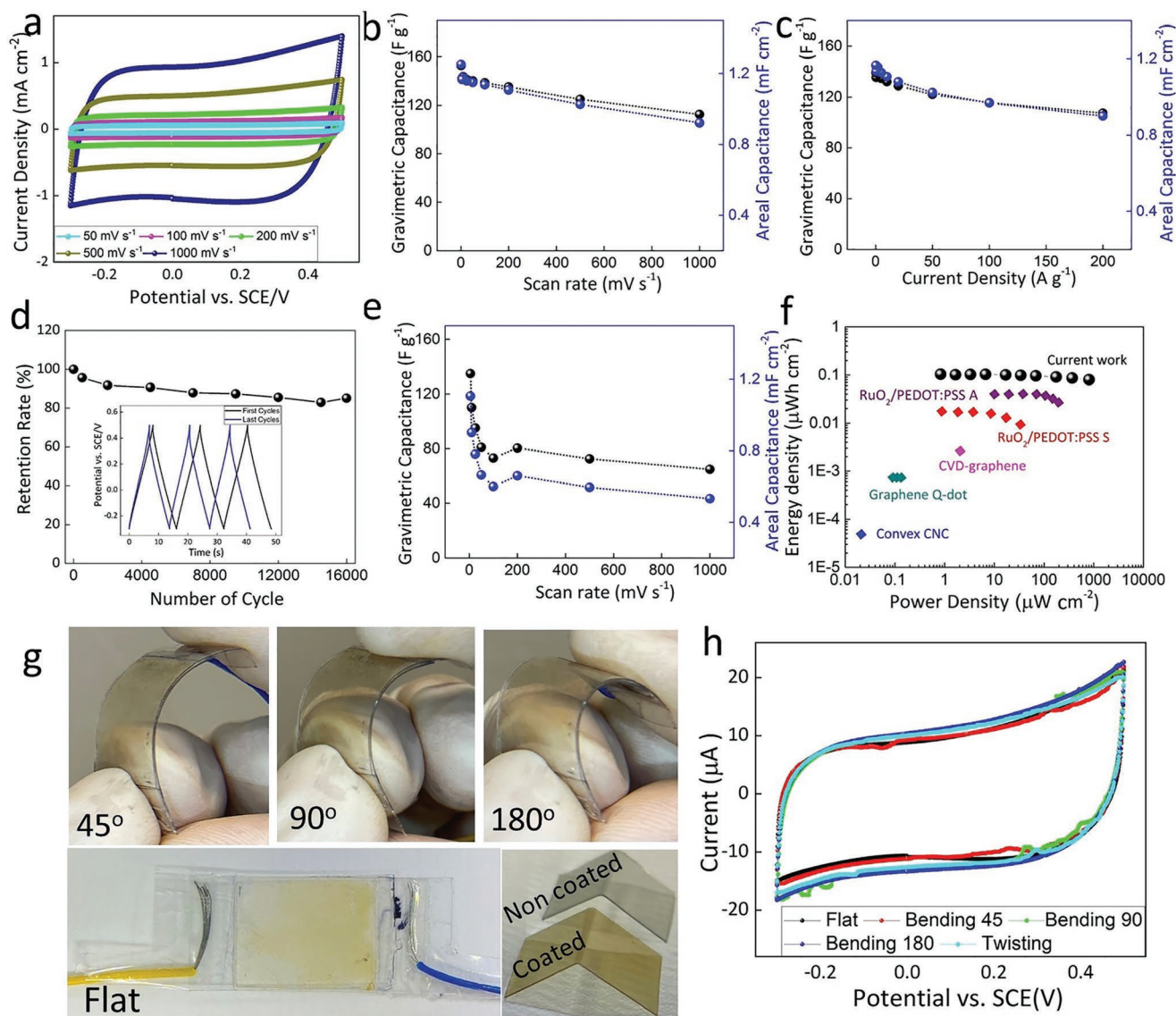
Figure 6. The results of the symmetric two-electrode ($Mn_{1-x-y}(Ce_xLa_y)O_{2-\delta}$ film coated on FTO) cell in 2 M KOH aqueous solution and room temperature: a) CVs at different scan rates, b) gravimetric and areal capacitances as a function of scan rate, c) gravimetric and areal capacitances as a function of current density, and d) stability performance at a current density of 10 A g^{-1}. The results of $Mn_{1-x-y}(Ce_xLa_y)O_{2-\delta}$ ultrathin film (deposited on FTO substrate) solid-state symmetric device: e) areal and gravimetric capacitances as a function of scan rate, and f) Ragone plot along with values for other devices developed in the literature. The results of the flexible solid-state symmetric two-electrode cell (the films deposited on ITO coated flexible PET); g) photographs of the pseudocapacitor, h) CVs after twisting and bending.

recently for flexible ultrathin films, as shown in Figure 6f. Both the power and energy densities exhibited high values compared with those reported from benchmark pseudocapacitor devices (either symmetric or asymmetric), including RuO$_2$/PEDOT:PSS,[4] carbon nanocap (CNC),[31] pristine graphene,[89] and reduced multilayer graphene oxide (RMGO).[89] In addition, three comparative tables have been prepared to compare the results of the present study (including the resistivity, capacitance, cycling stability, and the material) with literature, which are available in Tables S4–S6, Supporting Information.

A flexible and transparent device was also fabricated by controllable deposition of the $Mn_{1-x-y}(Ce_xLa_y)O_{2-\delta}$ on an ITO-coated flexible PET substrate while also using the solid electrolyte, as shown in Figure 6g. The energy and power densities of the ultrathin film-based flexible device were measured using CV analysis in a wide range of scan rates between 5 and 1000 mV s^{-1}. The results are shown in Figure S9c,d, Supporting Information. As a flexible and portable capacitor device, the variations of the electrochemical performance upon twisting and bending of electrodes at different angles of 45°, 90°, and 180° (Figure 6g) were explored. Figure 6h shows that the CV area remains unaffected during the twisting and bending, which illustrates the mechanical stability of the device. Furthermore, the inset of Figure 6g and Videos S1 and S2, Supporting Information, depict a full comparative analysis of the

coated and uncoated substrates. These experiments revealed high homogeneity, transparency, flexibility, and remarkable adherence of the film even after complete folding of the substrate. Such excellent mechanical flexibility and stability of the device as well as the strong adherence of the film on the substrate, even after vigorous bending and twisting, unveils great potential for the use of these advanced functional materials for state-of-the-art flexible and transparent pseudocapacitance applications.

3. Conclusion

The present work demonstrated the fabrication of flexible, transparent $Mn_{1-x-y}(Ce_xLa_y)O_{2-\delta}$ pseudocapacitor devices using a spent-batteries-derived precursor. A representative ultrathin film with high transmittance of 86% exhibited excellent areal and gravimetric capacitances of 3.4 mF cm^{-2} and 720 F g^{-1}. The excellent electrochemical performance was mainly ascribed to the anionic intercalation/de-intercalation of O^{2-} into the atomic tunnels of $Mn_{1-x-y}(Ce_xLa_y)O_{2-\delta}$ crystal structure, which is the first report for an oxide-based pseudocapacitor. Further, the $Mn_{1-x-y}(Ce_xLa_y)O_{2-\delta}$ yielded an outstanding capacitance retention of ≈90% after 16 000 cycles, which can be ascribed to the rapid redox reactions between the multivalence oxidation states of extrinsic Ce^{3+}, Ce^{4+}, and La^{3+} ions at the interstitial sites and intrinsic Mn ions in $Mn_{1-x-y}(Ce_xLa_y)O_{2-\delta}$ lattice. Such rapid exchange in oxidation states resulted in the retention of Mn cations with low oxidation states (i.e., Mn^{2+} and Mn^{3+}) during long-term cycling. Further, the electrochemical performance of a representative symmetric full-cell $Mn_{1-x-y}(Ce_xLa_y)O_{2-\delta}$ pseudocapacitor with a solid-state electrolyte was tested under twisting and bending conditions at 45°, 90°, and 180°, where no significant attenuation in performance was recorded. The present work establishes a new pathway to synthesize TMO-based pseudocapacitors with engineered defects and electronic properties to obtain pseudocapacitors with the desired flexibility, transparency, and cycling stability suitable for size-sensitive, portable, and wearable power-integrated electronic devices.

4. Experimental Section

A detailed description of fabrication processes, mechanisms, characterizations, computational studies, and additional analysis can be found in the Supporting Information.

Supporting Information

Supporting Information is available from the Wiley Online Library or from the author.

Acknowledgements

Conflict of Interest

The authors declare no conflict of interest.

Data Availability Statement

The data that supports the findings of this study are available in the supplementary material of this article.

Keywords

[1] B. Xie, Y. Wang, W. Lai, W. Lin, Z. Lin, Z. Zhang, P. Zou, Y. Xu, S. Zhou, C. Yang, F. Kang, C.-P. Wong, *Nano Energy* **2016**, *26*, 276.

[2] Z. Lei, J. Zhang, L. L. Zhang, N. A. Kumar, X. S. Zhao, *Energy Environ. Sci.* **2016**, *9*, 1891.

[3] Y.-H. Liu, J.-L. Xu, X. Gao, Y.-L. Sun, J.-J. Lv, S. Shen, L.-S. Chen, S.-D. Wang, *Energy Environ. Sci.* **2017**, *10*, 2534.

[4] C. Zhang, T. M. Higgins, S.-H. Park, S. O'Brien, D. Long, J. Coleman, V. Nicolosi, *Nano Energy* **2016**, *28*, 495.

[5] J. Chen, Y. Huang, N. Zhang, H. Zou, R. Liu, C. Tao, X. Fan, Z. L. Wang, *Nat. Energy* **2016**, *1*, 16138.

[6] D. J. Lipomi, B. C.-K. Tee, M. Vosgueritchian, Z. Bao, *Adv. Mater.* **2011**, *23*, 1771.

[7] X. Y. Liu, Y. Q. Gao, G. W. Yang, *Nanoscale* **2016**, *8*, 4227.

[8] T. Chen, Y. Xue, A. K. Roy, L. Dai, *ACS Nano* **2014**, *8*, 1039.

[9] P. Xu, J. Kang, J.-B. Choi, J. Suhr, J. Yu, F. Li, J.-H. Byun, B.-S. Kim, T.-W. Chou, *ACS Nano* **2014**, *8*, 9437.

[10] S. S. Delekta, A. D. Smith, J. Li, M. Östling, *Nanoscale* **2017**, *9*, 6998.

[11] N. Li, G. Yang, Y. Sun, H. Song, H. Cui, G. Yang, C. Wang, *Nano Lett.* **2015**, *15*, 3195.

[12] X. Yang, W. Peng, K. Fu, L. Mao, J. Jin, S. Yang, G. Li, *Electrochim. Acta* **2020**, *340*, 135989.

[13] Y. Zhong, X. Zhang, Y. He, H. Peng, G. Wang, G. Xin, *Adv. Funct. Mater.* **2018**, *28*, 1801998.

[14] C. (John) Zhang, V. Nicolosi, *Energy Storage Mater.* **2019**, *16*, 102.

[15] C. (John) Zhang, B. Anasori, A. Seral-Ascaso, S.-H. Park, N. McEvoy, A. Shmeliov, G. S. Duesberg, J. N. Coleman, Y. Gogotsi, V. Nicolosi, *Adv. Mater.* **2017**, *29*, 1702678.

[16] X. Jiao, C. Zhang, Z. Yuan, *ACS Appl. Mater. Interfaces* **2018**, *10*, 41299.

[17] K. Devarayan, D. Lei, H.-Y. Kim, B.-S. Kim, *Chem. Eng. J.* **2015**, *273*, 603.

[18] T. Cheng, Y.-Z. Zhang, J.-D. Zhang, W.-Y. Lai, W. Huang, *J. Mater. Chem. A* **2016**, *4*, 10493.

[19] T. M. Higgins, J. N. Coleman, *ACS Appl. Mater. Interfaces* **2015**, *7*, 16495.

[20] M. A. Borysiewicz, M. Ekielski, Z. Ogorzałek, M. Wzorek, J. Kaczmarski, T. Wojciechowski, *Nanoscale* **2017**, *9*, 7577.

[21] F. Liu, X. Yang, Z. Qiao, L. Zhang, B. Cao, G. Duan, *Electrochim. Acta* **2018**, *260*, 281.

[22] X. Liu, J. Wang, G. Yang, *Chem. Eng. J.* **2018**, *347*, 101.

[23] P. Suktha, N. Phattharasupakun, M. Sawangphruk, *Sustainable Energy Fuels* **2018**, *2*, 1799.

**ADVANCED
SCIENCE NEWS**

www.advancedsciencenews.com

**ADVANCED
FUNCTIONAL
MATERIALS**

www.afm-journal.de

[24] L. Shen, L. Du, S. Tan, Z. Zang, C. Zhao, W. Mai, *Chem. Commun.* **2016**, *52*, 6296.

[25] A. K. Sundramoorthy, Y.-C. Wang, S. Gunasekaran, *Nano Res.* **2015**, *8*, 3430.

[26] R. Yuksel, Z. Sarioba, A. Cirpan, P. Hiralal, H. E. Unalan, *ACS Appl. Mater. Interfaces* **2014**, *6*, 15434.

[27] H. Moon, H. Lee, J. Kwon, Y. D. Suh, D. K. Kim, I. Ha, J. Yeo, S. Hong, S. H. Ko, *Sci. Rep.* **2017**, *7*, 41981.

[28] H. Sheng, X. Zhang, Y. Ma, P. Wang, J. Zhou, Q. Su, W. Lan, E. Xie, C. Zhang, *ACS Appl. Mater. Interfaces* **2019**, *11*, 8992.

[29] S. Kiruthika, C. Sow, G. U. Kulkarni, *Small* **2017**, *13*, 1701906.

[30] Y. Wang, W. Zhou, Q. Kang, J. Chen, Y. Li, X. Feng, D. Wang, Y. Ma, W. Huang, *ACS Appl. Mater. Interfaces* **2018**, *10*, 27001.

[31] H. Y. Jung, M. B. Karimi, M. G. Hahm, P. M. Ajayan, Y. J. Jung, *Sci. Rep.* **2012**, *2*, 773.

[32] T. Qiu, B. Luo, M. Giersig, E. M. Akinoglu, L. Hao, X. Wang, L. Shi, M. Jin, L. Zhi, *Small* **2014**, *10*, 4136.

[33] Y.-H. Liu, J.-L. Xu, S. Shen, X.-L. Cai, L.-S. Chen, S.-D. Wang, *J. Mater. Chem. A* **2017**, *5*, 9032.

[34] T. Cheng, Y.-Z. Zhang, J.-P. Yi, L. Yang, J.-D. Zhang, W.-Y. Lai, W. Huang, *J. Mater. Chem. A* **2016**, *4*, 13754.

[35] I. Nam, S. Park, G.-P. Kim, J. Park, J. Yi, *Chem. Sci.* **2013**, *4*, 1663.

[36] A. Ferris, S. Garbarino, D. Guay, D. Pech, *Adv. Mater.* **2015**, *27*, 6625.

[37] D. L. Ma, Y. Ma, Z. W. Chen, A. M. Hu, *J. Mater. Chem. A* **2017**, *5*, 20608.

[38] W. Song, J. Zhu, B. Gan, S. Zhao, H. Wang, C. Li, J. Wang, *Small* **2018**, *14*, 1702249.

[39] J. Ge, G. Cheng, L. Chen, *Nanoscale* **2011**, *3*, 3084.

[40] K. Gao, Z. Shao, X. Wu, X. Wang, Y. Zhang, W. Wang, F. Wang, *Nanoscale* **2013**, *5*, 5307.

[41] T. Chen, H. Peng, M. Durstock, L. Dai, *Sci. Rep.* **2014**, *4*, 3612.

[42] P. Kanninen, N. D. Luong, L. H. Sinh, I. V. Anoshkin, A. Tsapenko, J. Seppälä, A. G. Nasibulin, T. Kallio, *Nanotechnology* **2016**, *27*, 235403.

[43] Z. M. Chan, D. A. Kitchaev, J. N. Weker, C. Schnedermann, K. Lim, G. Ceder, W. Tumas, M. F. Toney, D. G. Nocera, *Proc. Natl. Acad. Sci. U. S. A.* **2018**, *115*, E5261.

[44] L. Yang, S. Cheng, J. Wang, X. Ji, Y. Jiang, M. Yao, P. Wu, M. Wang, J. Zhou, M. Liu, *Nano Energy* **2016**, *30*, 293.

[45] M. Sun, B. Lan, T. Lin, G. Cheng, F. Ye, L. Yu, X. Cheng, X. Zheng, *CrystEngComm* **2013**, *15*, 7010.

[46] T. Gao, H. Fjellvåg, P. Norby, *Anal. Chim. Acta* **2009**, *648*, 235.

[47] A. Ramírez, P. Hillebrand, D. Stellmach, M. M. May, P. Bogdanoff, S. Fiechter, *J. Phys. Chem. C* **2014**, *118*, 14073.

[48] M. Huang, F. Li, F. Dong, Y. X. Zhang, L. L. Zhang, *J. Mater. Chem. A* **2015**, *3*, 21380.

[49] Z. Y. Leong, H. Y. Yang, *ACS Appl. Mater. Interfaces* **2019**, *11*, 13176.

[50] K. Chen, W. Pan, D. Xue, *J. Phys. Chem. C* **2016**, *120*, 20077.

[51] Y. Yuan, S. M. Wood, K. He, W. Yao, D. Tompsett, J. Lu, A. Nie, M. S. Islam, R. Shahbazian-Yassar, *ACS Nano* **2016**, *10*, 539.

[52] S. Devaraj, N. Munichandraiah, *J. Phys. Chem. C* **2008**, *112*, 4406.

[53] D. A. Tompsett, S. C. Parker, M. S. Islam, *J. Am. Chem. Soc.* **2014**, *136*, 1418.

[54] L. Wang, Y. Yu, H. He, Y. Zhang, X. Qin, B. Wang, *Sci. Rep.* **2017**, *7*, 12845.

[55] W. Zhang, Z. Yang, Y. Liu, S. Tang, X. Han, M. Chen, *J. Cryst. Growth* **2004**, *263*, 394.

[56] O. Ghodbane, F. Ataherian, N.-L. Wu, F. Favier, *J. Power Sources* **2012**, *206*, 454.

[57] Z. Hu, X. Xiao, C. Chen, T. Li, L. Huang, C. Zhang, J. Su, L. Miao, J. Jiang, Y. Zhang, J. Zhou, *Nano Energy* **2015**, *11*, 226.

[58] S. S. Mofarah, E. Adabifiroozjaei, Y. Yao, P. Koshy, S. Lim, R. Webster, X. Liu, R. K. Nekouei, C. Cazorla, Z. Liu, Y. Wang, N. Lambropoulos, C. C. Sorrell, *Nat. Commun.* **2019**, *10*, 2594.

[59] K. S. Kumar, J. Cherusseri, J. Thomas, *ACS Omega* **2019**, *4*, 4472.

[60] B. A. Mei, J. Lau, T. Lin, S. H. Tolbert, B. S. Dunn, L. Pilon, *J. Phys. Chem. C* **2018**, *122*, 24499.

[61] T. Gu, B. Wei, *Nanoscale* **2015**, *7*, 11626.

[62] J. Creus, F. Brezault, C. Rebere, M. Gadouleau, *Surf. Coat. Technol.* **2006**, *200*, 4636.

[63] A. Buffa, D. Mandler, *Electrochim. Acta* **2019**, *318*, 496.

[64] P. J. King, T. M. Higgins, S. De, N. Nicoloso, J. N. Coleman, *ACS Nano* **2012**, *6*, 1732.

[65] A. Ponzoni, *Appl. Phys. Lett.* **2019**, *114*, 153105.

[66] P. Salles, E. Quain, N. Kurra, A. Sarycheva, Y. Gogotsi, *Small* **2018**, *14*, 1802864.

[67] E. Jokar, S. Shahrokhian, A. I. zad, E. Asadian, H. Hosseini, *J. Energy Storage* **2018**, *17*, 465.

[68] B. Ruzicka, L. Degiorgi, R. Gaal, L. Thien-Nga, R. Bacsa, J. Salvetat, L. Forró, *Phys. Rev. B: Condens. Matter Mater. Phys.* **2000**, *61*, R2468.

[69] E. M. Doherty, S. De, P. E. Lyons, A. Shmeliov, P. N. Nirmalraj, V. Scardaci, J. Joimel, W. J. Blau, J. J. Boland, J. N. Coleman, *Carbon* **2009**, *47*, 2466.

[70] S. De, P. J. King, M. Lotya, A. O'Neill, E. M. Doherty, Y. Hernandez, G. S. Duesberg, J. N. Coleman, *Small* **2010**, *6*, 458.

[71] M. Toupin, T. Brousse, D. Bélanger, *Chem. Mater.* **2004**, *16*, 3184.

[72] X. Lang, A. Hirata, T. Fujita, M. Chen, *Nat. Nanotechnol.* **2011**, *6*, 232.

[73] C.-C. Hu, K.-H. Chang, M.-C. Lin, Y.-T. Wu, *Nano Lett.* **2006**, *6*, 2690.

[74] H. Lindström, S. Södergren, A. Solbrand, H. Rensmo, J. Hjelm, A. Hagfeldt, S.-E. Lindquist, *J. Phys. Chem. B* **1997**, *101*, 7717.

[75] V. Augustyn, J. Come, M. A. Lowe, J. W. Kim, P.-L. Taberna, S. H. Tolbert, H. D. Abruña, P. Simon, B. Dunn, *Nat. Mater.* **2013**, *12*, 518.

[76] J. T. Mefford, W. G. Hardin, S. Dai, K. P. Johnston, K. J. Stevenson, *Nat. Mater.* **2014**, *13*, 726.

[77] H. P. Boehm, *Discuss. Faraday Soc.* **1971**, *52*, 264.

[78] Y. Liu, S. P. Jiang, Z. Shao, *Mater. Today Adv.* **2020**, *7*, 100072.

[79] J.-L. Shi, D.-D. Xiao, M. Ge, X. Yu, Y. Chu, X. Huang, X.-D. Zhang, Y.-X. Yin, X.-Q. Yang, Y.-G. Guo, L. Gu, L.-J. Wan, *Adv. Mater.* **2018**, *30*, 1705575.

[80] D. Chen, D. Ding, X. Li, G. H. Waller, X. Xiong, M. A. El-Sayed, M. Liu, *Chem. Mater.* **2015**, *27*, 6608.

[81] R. Dong, Q. Ye, L. Kuang, X. Lu, Y. Zhang, X. Zhang, G. Tan, Y. Wen, F. Wang, *ACS Appl. Mater. Interfaces* **2013**, *5*, 9508.

[82] X. Li, X. Ma, D. Su, L. Liu, R. Chisnell, S. P. Ong, H. Chen, A. Toumar, J. C. Idrobo, Y. Lei, J. Bai, F. Wang, J. W. Lynn, Y. S. Lee, G. Ceder, *Nat. Mater.* **2014**, *13*, 586.

[83] F. Ning, B. Xu, J. Shi, H. Su, M. Wu, G. Liu, C. Ouyang, *J. Mater. Chem. A* **2017**, *5*, 9618.

[84] T. Ohzuku, J. Kato, K. Sawai, T. Hirai, *J. Electrochem. Soc.* **1991**, *138*, 2556.

[85] Z. Wang, Q. Qin, W. Xu, J. Yan, Y. Wu, *ACS Appl. Mater. Interfaces* **2016**, *8*, 18078.

[86] S. Zhang, N. Pan, *Adv. Energy Mater.* **2015**, *5*, 1401401.

[87] V. Khomenko, E. Frackowiak, F. Béguin, *Electrochim. Acta* **2005**, *50*, 2499.

[88] A. Varzi, R. Raccichini, S. Passerini, B. Scrosati, *J. Mater. Chem. A* **2016**, *4*, 17251.

[89] J. J. Yoo, K. Balakrishnan, J. Huang, V. Meunier, B. G. Sumpter, A. Srivastava, M. Conway, A. L. M. Reddy, J. Yu, R. Vajtai, P. M. Ajayan, *Nano Lett.* **2011**, *11*, 1423.